Title

Alkyne-Functionalized Platinum Chalcogenide (S, Se) Nanoparticles

Journal

Inorganic Chemistry, 63(2)

ISSN

0020-1669

Authors

Liu, Qiming

Song, Xingjian

DuBois, Davida

et al.

Publication Date

2024-01-15

DOI

10.1021/acs.inorgchem.3c03386

Inorganic Chemistry

pubs.acs.org/IC Article

Alkyne-Functionalized Platinum Chalcogenide (S, Se) Nanoparticles

Qiming Liu,[§] Xingjian Song,[§] Davida DuBois, Bingzhe Yu, Amrinder Bhuller, Gabriel Flannery, Marcus Hawley, Frank Bridges, and Shaowei Chen*

Cite This: *Inorg. Chem.* 2024, 63, 1046−1053 Read Online

ACCESS | Metrics & More | Article Recommendations | Supporting Information

ABSTRACT: Metal chalcogenide nanoparticles play a vital role in a wide range of applications and are typically stabilized by organic derivatives containing thiol, amine, or carboxyl moieties, where the nonconjugated particle−ligand interfaces limit the electronic interactions between the inorganic cores and organic ligands. Herein, a wet-chemistry method is developed for the facile preparation of stable platinum chalcogenide (S, Se) nanoparticles capped with acetylene derivatives (e.g., 4-ethylphenylacetylene, EPA). The formation of Pt−C≡ conjugated bonds at the nanoparticle interfaces, which is confirmed by optical and X-ray spectroscopic measurements, leads to markedly enhanced electronic interactions between the d electrons of the nanoparticle cores and π electrons of the acetylene moiety, in stark contrast to the mercapto-capped counterparts with only nonconjugated Pt−S− interfacial bonds, as manifested in spectroscopic measurements and density functional theory calculations. This study underscores the significance of conjugated anchoring linkages in the stabilization and functionalization of metal chalcogenides, a unique strategy for diverse applications.

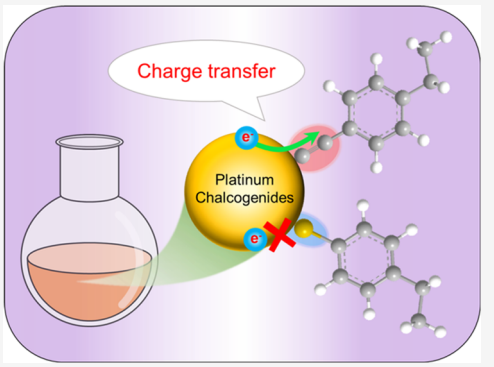

INTRODUCTION

Metal chalcogenide nanoparticles have been attracting extensive attention, due to their unique optical and electronic properties and significant potential in various applications, such as optoelectronics, photovoltaics, catalysis, energy storage, and biomedicine.[1−5] These nanoparticles are typically synthesized via colloidal, hydro/solvothermal heating methods and stabilized by select organic ligands,[6−9] such as derivatives of thiol (−SH), phosphine oxide (O═PR_3), phosphonyl (−$PO(OR)_2$), amine (−NH_2), and carboxyl (−COOH), leading to ready manipulation of their hydrophilicity, surface charge, tensile stress, dipole moment, catalytic performance, etc.[4,10−12] Yet in these earlier studies, the ligands are bound onto the nanoparticles mostly by nonconjugated interfacial linkages, which drastically limit the electronic coupling between the inorganic cores and organic functional moieties.[13−15] Such electronic interactions are anticipated to be markedly enhanced with conjugated interfacial points of anchor. This has indeed been demonstrated with acetylene-functionalized metal nanoparticles/clusters, where the hybridization between the π electrons of the acetylene moiety and metal d electrons leads to strong intraparticle charge delocalization.[16−21]

Notably, conjugated alkynyl functionalization has also been extended to semiconductor nanoparticles. For example, alkene and alkyne ligands have been used to modify Si nanoparticles, and the formation of conjugated interfacial linkages (i.e., Si−CH═CH−, Si−C≡C−) results in enhanced photoemission, electrical conductivity, and thermoelectric activity, compared to the nonconjugated counterparts.[22−24] In another study,[25] metal oxide nanoparticles, such as TiO_2, were functionalized with acetylene derivatives via a facile sol−gel method, where the resulting Ti−O−C≡C− interfacial bonds led to the generation of an interfacial state (IS) between the valence band (VB) and conduction band (CB) and hence efficient charge transfer across the core−ligand interface and improved photocatalytic activity, in stark contrast to the carboxylic ligand-capped counterparts. Such unique chemistry was also exploited for the first-ever preparation of stable cuprous hydroxide (CuOH) nanostructures,[26] where the formation of Cu−C≡C− interfacial bonds led to effective core−ligand electronic coupling and a drastically narrowed bandgap. This facilitated the production of hydroxyl radicals under photoirradiation for antimicrobial applications, as compared to the mercapto-capped counterparts. One immediate question arises: can alkyne ligands be used to stabilize metal chalcogenide nanoparticles as well? Such surface functionalization will enrich the toolbox for the deliberate manipulation of the materials' optical/electronic properties, a critical first step toward their diverse applications.

Herein, for the first time ever, alkyne-protected platinum chalcogenide (PtS_x and $PtSe_x$) nanoparticles were prepared by

Received: September 27, 2023
Revised: December 12, 2023
Accepted: December 12, 2023
Published: January 3, 2024

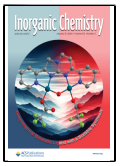

https://doi.org/10.1021/acs.inorgchem.3c03386
Inorg. Chem. 2024, 63, 1046−1053

a simple wet-chemical method. Experimentally, 4-ethylphenylacetylene (EPA) was first mixed with Pt(II) ions in dimethyl sulfoxide (DMSO), and Pt chalcogenide nanoparticles of ca. 2 nm in diameter were produced upon the addition of chalcogen anions. Notably, the EPA-capped Pt chalcogenide nanoparticles demonstrated unique photoluminescence and interfacial charge transfer properties, compared to the nanoparticles capped with 4-ethylphenylthiol (EPT). This was ascribed to the formation of conjugated Pt−C≡C−metal−ligand interfacial bonding interactions in the former, in contrast to the nonconjugated Pt−S linkage in the latter.

RESULTS AND DISCUSSION

The synthesis of alkyne-capped noble metal chalcogenide nanoparticles involves two major steps, as shown in Figure 1a.

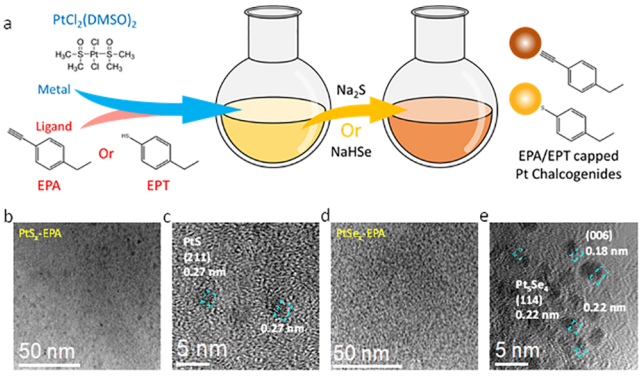

Figure 1. (a) Schematic of the synthesis of alkyne/thiol-functionalized noble metal chalcogenide nanoparticles. Representative TEM images of (b, c) PtS_x-EPA and (d, e) $PtSe_x$-EPA.

First, metal complexes of $PtCl_2(DMSO)_2$ were dissolved in DMSO, along with a calculated amount of the EPA or EPT ligands. Then, an aqueous solution of sodium chalcogenide (S or Se) was added dropwise into the reaction vessel, where the solution exhibited a rapid color change from yellow to dark brown (Figures S1 and S2), signifying the formation of organically capped Pt chalcogenide nanoparticles. The samples were denoted as PtS_x-EPA, PtS_x-EPT, $PtSe_x$-EPA, and $PtSe_x$-EPT nanoparticles and could be readily dispersed in nonpolar solvents such as dichloromethane (DCM), tetrahydrofuran (THF), toluene, etc. Notably, the sulfide samples remained stable, while precipitation occurred in the selenide samples after 2 weeks, possibly due to the loss of ligands from the nanoparticle surface (Figure S3). The details are included in the Experimental Section.

Transmission electron microscopy (TEM) was first employed to characterize the structures of the nanoparticles. As shown in Figures 1b−e, S4, and S5, all samples consist of nanoparticles of 2−3 nm in diameter (Figure S6). For PtS_x-EPA (Figure 1c) and PtS_x-EPT (Figure S4b) nanoparticles, well-defined lattice fringes can be readily identified in high-resolution measurements, featuring an interplanar spacing of ca. 0.27 nm, which can be ascribed to the (211) facets of tetragonal PtS (ICSD #649539).[27] Clear lattice fringes can also be seen in high-resolution TEM measurements of the $PtSe_x$-EPA nanoparticles (Figure 1d,e), where the interplanar spacings of 0.22 and 0.18 nm are consistent with the (114) and (006) facets of monoclinic Pt_5Se_4, respectively. For the $PtSe_x$-EPT sample (Figure S5a), lattice fringes with *d*-spacings of 0.21 and 0.32 nm can be readily resolved (Figure S5b), corresponding to the (114) and (11$\bar{2}$) facets of Pt_5Se_4 (ICSD #87926).[28] Because of the ultrasmall size of the nanoparticles, no clear diffraction patterns can be observed in the X-ray diffraction (XRD) measurements (Figure S7).

In elemental mapping measurements based on energy-dispersive X-ray spectroscopy (EDS), the elements of Pt, C, S, or Se can be clearly resolved in the samples of PtS_x-EPA (Figure S8), PtS_x-EPT (Figure S9), $PtSe_x$-EPA (Figure S10), and $PtSe_x$-EPT (Figure S11). Additionally, the Pt/S atomic ratio was estimated to be ca. 1:1.5 for PtS_x-EPA and 1:2.5 for PtS_x-EPT, and the Pt/Se ratio was 1:1.5 for $PtSe_x$-EPA and 1:1 for $PtSe_x$-EPT.

The elemental composition and valency of the Pt chalcogenide nanoparticles were then probed by X-ray photoelectron spectroscopy (XPS) measurements. From the survey spectra in Figure S12, the Se 3d, Pt 4f, S 2p, C 1s, and O 1s electrons can be readily identified in the samples at ca. 53, 72, 162, 284, and 532 eV, and based on the integrated peak areas, the atomic ratio of Pt/X was estimated to be around 1:1.5 for both PtS_x-EPA and $PtSe_x$-EPA, whereas the Pt/S ratio was ca. 1:2.5 for PtS_x-EPT and 1.4 for $PtSe_x$-EPT (with the Pt/Se ratio of 1:1.3, Figure S13) (Tables S1−S4), consistent with the results obtained from EDS measurements (Figures S8−S11). One can see that these are higher than the stoichiometric ratio of the respective chalcogenides (i.e., PtS and Pt_5Se_4), suggesting the formation of chalcogenide-rich nanoparticle cores.

From the high-resolution scans of the Pt 4f electrons in Figure 2a, a doublet can be resolved at ca. 72.05/75.25 eV for both PtS_x-EPA and $PtSe_x$-EPA, with a spin−orbit coupling of ca. 3.2 eV, which can be ascribed to the $4f_{7/2}$ and $4f_{5/2}$ electrons of Pt^{2+}.[29] These binding energies were ca. 0.5 and 0.3 eV higher than those of PtS_x-EPT (71.58/74.78 eV) and $PtSe_x$-EPT (71.71/74.91 eV). This suggests electron depletion in the PtS_x-EPA and $PtSe_x$-EPA samples, most likely due to electron transfer from the nanoparticle cores to the EPA ligands. Note that similar interfacial charge transfer was observed in our earlier study with acetylene-capped iridium nanoparticles but not with the mercapto-capped counterpart.[20]

Figure 2b depicts the high-resolution scans of the S 2p electrons for PtS_x-EPA and PtS_x-EPT, where a doublet can be resolved at 162.32/163.58 and 162.24/163.50 eV due to the $2p_{3/2}$ and $2p_{1/2}$ electrons of S^{2-},[30] respectively, again, consistent with the slightly electron-depleted Pt in the former compared to that in the latter. A similar phenomenon was observed with the high-resolution scan of the Se 3d electrons of $PtSe_x$-EPA and $PtSe_x$-EPT (Figure 2c), where the $3d_{5/2}$/$3d_{3/2}$ doublet of Se^{2-} were found at a slightly higher binding energy for the former (54.30/54.90 eV) than for the latter (54.20/54.88 eV).[31−33]

High-resolution scans of the C 1s electrons further confirmed the existence of EPA and EPT ligands on the Pt chalcogenide nanoparticle surfaces. From Figure S14, it can be seen that deconvolution of the C 1s spectra of the EPA-capped samples yields three species, sp C (from C≡C) at ca. 283.3 eV, sp^2 C (from C=C of the phenyl rings) at ca. 284.0 eV, and sp^3 C (from the ethyl moieties) at ca. 284.5 eV, which are consistent with the structure of the EPA ligand. As for the two EPT-capped samples, only sp^2 C and sp^3 C can be discerned in the spectra.[26] Meanwhile, as one can see from Figure S15, no peaks can be deconvoluted below 530.0 eV, suggesting the absence of metal oxides among all samples.[34]

https://doi.org/10.1021/acs.inorgchem.3c03386
Inorg. Chem. 2024, 63, 1046−1053

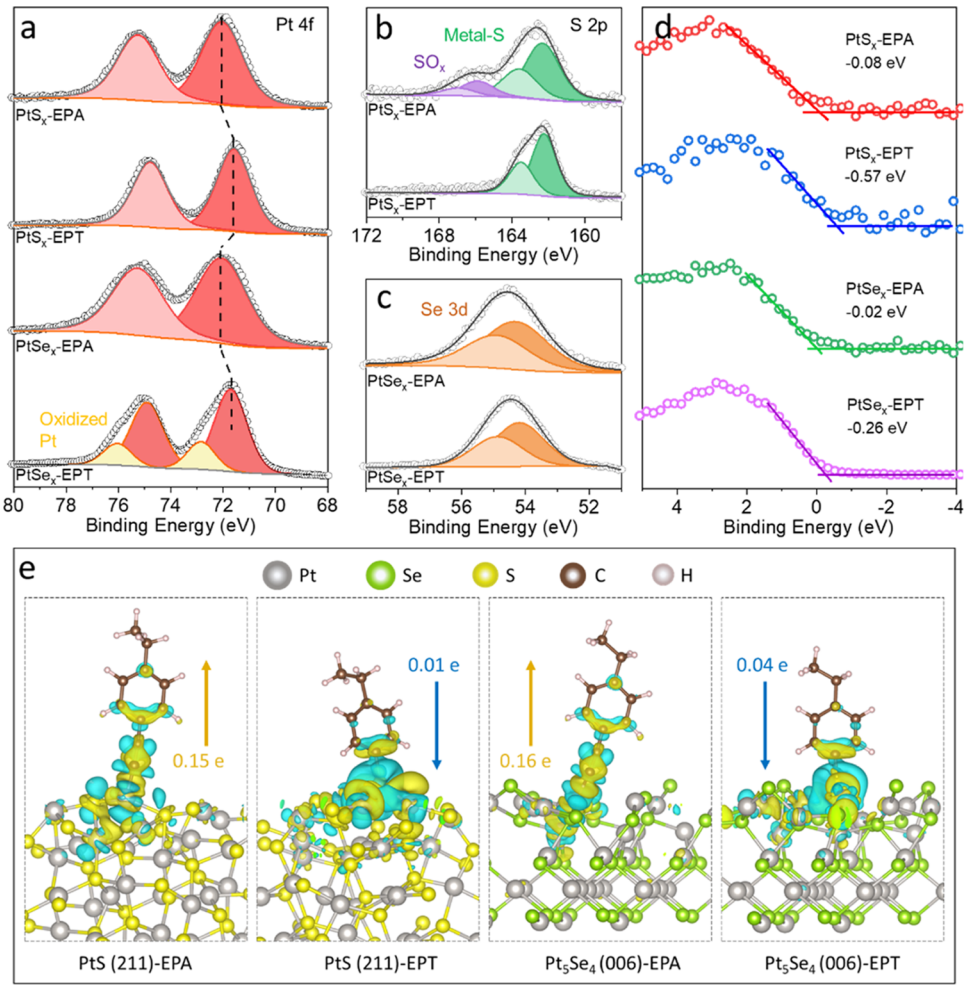

Figure 2. (a) High-resolution XPS spectra of the Pt 4f electrons of PtS_x-EPA, PtS_x-EPT, $PtSe_x$-EPA, and $PtSe_x$-EPT. High-resolution XPS spectra of (b) the S 2p electrons of PtS_x-EPA and PtS_x-EPT and (c) the Se 3d electrons of $PtSe_x$-EPA and $PtSe_x$-EPT. (d) VBM spectra of PtS_x-EPA, PtS_x-EPT, $PtSe_x$-EPA, and $PtSe_x$-EPT. (e) Bader charge analysis of PtS(211)-EPA, PtS(211)-EPT, Pt_5Se_4(006)-EPA, and Pt_5Se_4(006)-EPT. The cyan and yellow areas signify electron loss and electron gain, respectively. The isovalue of the charge density is 0.0015 e/au^3.

Notably, the valence band maximum (VBM) spectra of the samples display a consistent trend of charge transfer. As shown in Figure 2d, all samples possessed a negative VBM over the Fermi level (0 eV), indicating metallic/semimetallic band structures, which are typical for noble metal chalcogenides.[33,35,36] Specifically, the VBMs are estimated to be −0.08 and −0.09 eV for PtS_x-EPA and $PtSe_x$-EPA, and they are lower at −0.57 and −0.26 eV for the EPT-capped counterparts (PtS_x-EPT and $PtSe_x$-EPT), respectively. This suggests that the d band of the two EPA-capped samples shifted further away from the Fermi level, consistent with charge transfer from the nanoparticles to the ligands.

To further understand the charge transfer between the Pt chalcogenide cores and EPA/EPT ligands, Bader charge analysis based on DFT calculations was carried out using a model with a PtS(211) or Pt_5Se_4(006) facet capped with EPA or EPT ligands (Figures S16 and S17). One can see that efficient charge transfer occurs at the interface from the Pt chalcogenide core to the EPA ligands with both PtS (0.15 e) and Pt_5Se_4 (0.16 e), as depicted in Figure 2e. Charge accumulation (yellow color isosurfaces) can be found on the −C≡C− bonds of the EPA ligands, suggesting delocalization of the π electrons.[20] In contrast, EPT ligands actually induced interfacial charge transfer in the opposite direction, injecting a negligible amount of electrons into both PtS (0.01 e) and Pt_5Se_4 (0.04 e) cores. This is consistent with results from the above XPS measurements that Pt in the EPA-capped nanoparticles was more electron-deficient compared to the EPT-capped samples due to interfacial electron loss.

Furthermore, in comparison to bare PtS and Pt_5Se_4, density of states (DOS) analysis shows that the effects of ligand functionalization were mostly confined to the nanoparticle core surface, with essentially no change of the bulk properties (Figure S18). In addition, the DOS distributions are consistent with a conductive core, as suggested in the VBM spectra (Figure 2d). Nevertheless, in comparison to EPT-modified or bare PtS and Pt_5Se_4, the projected DOS (PDOS) showed a strong interaction between the d orbitals of the Pt atoms and the p orbitals of the C atoms of C≡C in EPA-modified PtS and Pt_5Se_4 (Figure S19). Strong σ and π bonds were formed, as shown in Figure S20, which led to the downward shift of the Pt d orbitals from the Fermi level due to electron loss from Pt to EPA ligands at the core−ligand interfaces.

Further structural insights were obtained from Fourier transform infrared (FTIR) spectroscopic measurements. From Figure 3a, one can see that all samples exhibited three major vibrational bands at 2870, 2920, and 2960 cm^{-1}, due to the CH_3/CH_2 stretches of the ethyl moieties of the EPA and EPT

https://doi.org/10.1021/acs.inorgchem.3c03386
Inorg. Chem. 2024, 63, 1046−1053

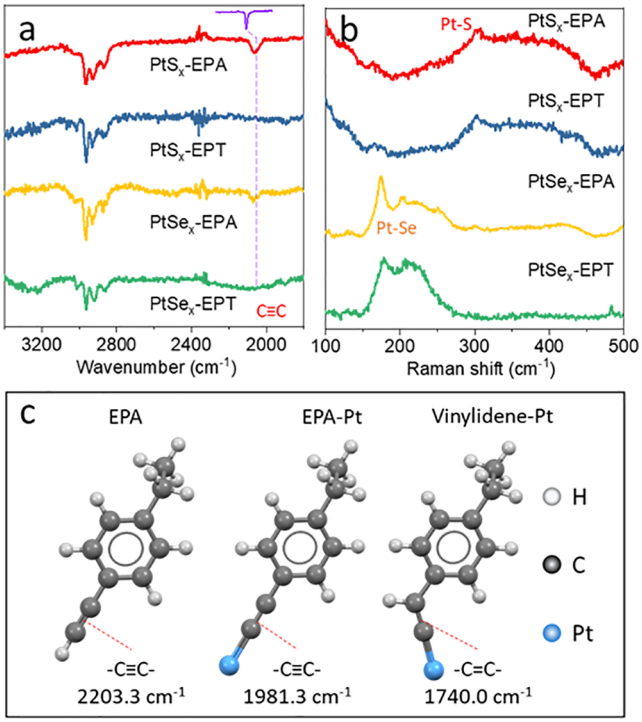

Figure 3. (a) FTIR spectra and (b) Raman spectra of PtS_x-EPA, PtS_x-EPT, $PtSe_x$-EPA, and $PtSe_x$-EPT. Purple line in panel (a) is the experimental data of −C≡C− in the EPA molecule. (c) Calculated vibrational frequency of anchoring linkage (−C≡C− or −C═C−) in the EPA molecule, EPA-Pt with Pt−C≡C− linkage, and EPA-Pt with vinylidene linkage.

ligands, along with a small peak at around 3020 cm^{-1} arising from the ═C−H stretch of the phenyl rings. For the EPA-capped samples, the C≡C vibration can be identified at 2063 cm^{-1}, corresponding to a red shift of 45 cm^{-1} compared to that of monomeric EPA ligands (2108 cm^{-1}, purple line in Figures 3a and S21). A similar C≡C vibration was observed with the mixture of the Pt and EPA precursors before the addition of S or Se sources (2073 cm^{-1}, Figure S22), suggesting that the formation of a Pt−EPA complex was the preliminary step in the synthesis of the acetylene-functionalized Pt chalcogenide nanoparticles. This is consistent with the formation of conjugated core−ligand bonding interactions that facilitate interfacial electronic coupling, leading to a reduced bonding order of the acetylene moiety. This is further confirmed in DFT calculations (Figures 3c and S23) where monomeric EPA ligands showed a C≡C vibration at 2203.3 cm^{-1}, which red-shifted by 222 to 1981.3 cm^{-1} when the terminal H was replaced with a Pt atom (Pt−C≡C−). Note that tautomeric rearrangement might occur from Pt−C≡C− to Pt═C═C−; the corresponding C═C vibration was anticipated to appear at 1740.0 cm^{-1} (Figure 3c), and for EPA ligands bonded to Pt in a side-on configuration (Figure S24), the resulting C═C vibration was expected at 1819.2 cm^{-1} due to π-interaction with the Pt atom. Yet none of these vibrations were observed in the experimental data. Taken together, these results suggest a Pt−C≡C− interfacial linkage in the EPA-capped nanoparticles, where π bonds were formed by the overlapping of the d_π orbital or $p_\pi d_\pi$ hybrid of the metal centers and the π^* orbital of the C_{sp} atoms of the EPA ligands.[18,19,37,38] In contrast, no such peak can be seen with the EPT-capped samples. Also, it should be noted that the stretching vibration of terminal H−C≡ (3292 cm^{-1}) or H−S− (2566 cm^{-1}) vanished from the nanoparticle samples, suggesting the absence of excessive EPA or EPT ligands in the nanoparticle samples, and the spectroscopical data were due to nanoparticle-bound ligands only.

Consistent results were obtained in proton nuclear magnetic resonance (^{1}H NMR) measurements of PtS_x-EPA and $PtSe_x$-EPA (Figure S25), where the spectral features for the phenyl (7.2 ppm), methylene (2.6 ppm), and methyl (1.2 ppm) protons were significantly broadened, whereas sharp splitting can be observed with the Pt−EPA complexes (Figure S26). The absence of peak splitting of PtS_x-EPA and $PtSe_x$-EPA indicates that the signals were from nanoparticle-bound ligands only and the samples were spectroscopically clean, as observed extensively with organically capped nanoparticles.[25,39]

In Raman spectroscopic measurements (Figure 3b), one can see that both PtS_x-EPA and PtS_x-EPT nanoparticles exhibited a peak at 304 cm^{-1} and a broad one from 300 to 450 cm^{-1}, which can be attributed to the E_{1g} and A_{1g} modes of the Pt−S vibrations, respectively.[40] As for $PtSe_x$-EPA and $PtSe_x$-EPT, two well-defined vibrations can be readily observed at 175 and 204 cm^{-1} due to the Pt−Se vibrations in E_{1g} and A_{1g} modes, respectively.[41] These results further confirmed the formation of Pt chalcogenide nanoparticles, which is consistent with the above TEM and XPS results.

Further structural information was provided by X-ray absorption spectroscopy (XAS) measurements. Figure 4a depicts the Pt LIII-edge X-ray absorption near-edge spectra (XANES) of the obtained Pt chalcogenide nanoparticles, where the absorption edge energy is seen to increase in the order of Pt foil < $PtSe_x$-EPA ≈ $PtSe_x$-EPT < PtS_x-EPT < PtS_x-EPA (Figure 4a inset), consistent with results from XPS measurements that functionalization with the EPA ligands

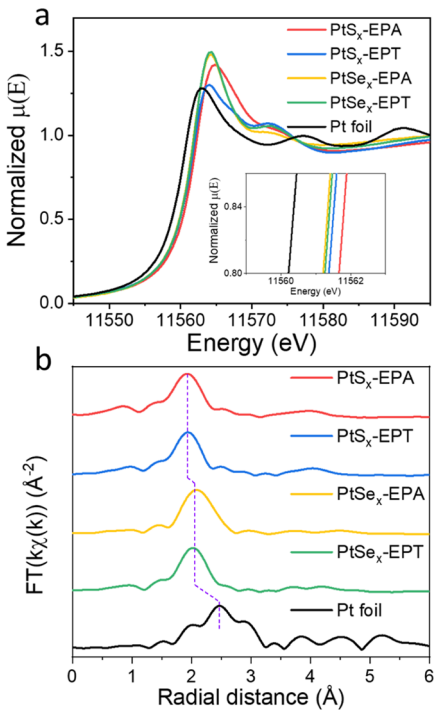

Figure 4. XAS measurements. (a) XANES of the Pt LIII-edge and (b) the corresponding EXAFS for PtS_x-EPA, PtS_x-EPT, $PtSe_x$-EPA, $PtSe_x$-EPT, and Pt foil. The inset to panel (a) is the zoom-in of the edges of the samples.

https://doi.org/10.1021/acs.inorgchem.3c03386
Inorg. Chem. 2024, 63, 1046−1053

facilitated interfacial charge transfer making the Pt centers electron-deficient, compared to the EPT-capped ones.

The corresponding Fourier transformed extended X-ray absorption fine structure (FT-EXAFS) spectra are shown in Figure 4b, where both PtS_x-EPA and PtS_x-EPT can be seen to possess only one major peak at 1.92 and 1.94 Å, respectively, due to the Pt−S path with a bond length of 2.32 Å and coordination number (CN) of 3.4 and 3.8, respectively (Figure S27a,b, Tables S5 and S6). $PtSe_x$-EPA also exhibited one main peak at 2.09 Å (Figure 4b) due to the Pt−Se bonds with a bond length of 2.45 Å and a CN of 4.7 (Figure S27c and Table S7). As for $PtSe_x$-EPT (Figure 4b), the Pt−Se peak shifted slightly to 2.03 Å (bond length 2.42 Å and CN 6.6) (Figure S27d and Table S8). These all exhibited a clear deviation from the first shell Pt−Pt bonds of Pt foil at 2.46 Å (bond length 2.78 Å and CN 12). Meanwhile, the absence of Pt−C at ca. 1.5 Å rules out the possibility of simple metal−acetylene organometallic complexes with S or Se in the samples (Figure S28).

The optical properties of the nanoparticles were then examined via UV−vis absorption measurements. One can see from Figure 5a that all samples exhibited an exponential decay

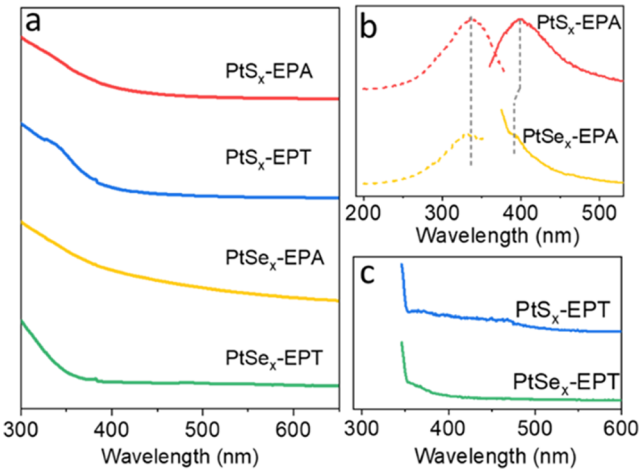

Figure 5. (a) UV−vis absorption and (b, c) PL spectra of (b) PtS_x-EPA and $PtSe_x$-EPA and (c) PtS_x-EPT and $PtSe_x$-EPT nanoparticles. Dashed curves in panel (b) represent the excitation spectra, and solid curves represent the emission spectra. The excitation spectra are acquired at the emission wavelengths of 398 and 390 nm for PtS_x-EPA and $PtSe_x$-EPA, respectively. The emission spectra are obtained at the excitation wavelength of 337 nm for all samples in panels (b) and (c).

profile, consistent with their nanosized structures, with an absorption threshold between 350 and 400 nm.[42] Interestingly, the EPA-capped nanoparticles also exhibited clear photoluminescence (PL) properties. Specifically, when excited at 337 nm, PtS_x-EPA showed an emission peak at 398 nm, in comparison to ca. 390 nm for $PtSe_x$-EPA (Figure 5b), in contrast to the EPA monomers that possessed an excitation maximum at 298 nm and emission maximum at 353 nm (Figure S29). The marked red shift of the emission of the former can be explained by the formation of Pt−C≡C interfacial bonds, which facilitated core−ligand charge delocalization by the hybridization of the metal d orbitals and π bonds of the EPA ligands, such that the PL was analogous to that of the diacetylene moiety (−C≡C−C≡C−).[19−21,38] Note that the Pt−EPA complex (Figure S22) also exhibited the same PL excitation and emission (Figure S30), suggesting effective mediation of the Pt center in inducing charge delocalization between the C≡C π bonds (Figure S31). By contrast, no PL emission was observed with the two EPT-capped nanoparticles (Figure 5c), as the nonconjugated interfacial linkages impeded electronic coupling at the core−ligand interface.

CONCLUSIONS

In summary, for the first time ever, we successfully synthesized platinum chalcogenide (S, Se) nanoparticles capped with acetylene derivatives forming Pt−C≡C− interfacial bonds. Such conjugated modifications lead to significant charge transfer between the ligands and the metal chalcogenide cores, in sharp contrast to thiol capping ligands that effectively impede interfacial charge transfer, as manifested in spectroscopic and computational studies. Significantly, such interfacial engineering can be extended to other metal chalcogenide nanoparticles (e.g., RuS_x-EPA and $RuSe_x$-EPA, Figures S32−S37, Tables S9 and S10). Results from these studies highlight the significance of conjugated interfacial linkages in the deliberate manipulation of the optoelectronic properties of metal chalcogenide nanoparticles.

EXPERIMENTAL SECTION

Chemicals. Cis-dichlorobis(dimethyl sulfoxide)platinum(II) (Pt-$(DMSO)_2Cl_2$, 97%, Sigma-Aldrich), sodium sulfide nonahydrate ($Na_2S{\cdot}9H_2O$, ≥99.99%, Sigma-Aldrich), Se powder (99.999%, TRI America), sodium borohydride ($NaBH_4$, 99%, Acros), EPA (97%, Acros), EPT (>97%, TCI America), and solvents were purchased from typical commercial sources and used without further purification. Water was purified using a Barnstead Nanopure water system (resistivity 18.3 MΩ·cm).

Nanoparticle Synthesis. Metal chalcogenide nanoparticles functionalized by alkyne ligands were synthesized by using DMSO colloidal dispersions.[43] Briefly, 0.1 mmol of $Pt(DMSO)_2Cl_2$ was dissolved in 20 mL of DMSO under sonication into a transparent solution in a round-bottom flask. Then, 100 μL of EPA ligands were added into the flask and heated at 80 °C under vigorous stirring for 1 h in an oil bath. After the solution was cooled down to 60 °C, 0.2 mmol of $Na_2S{\cdot}9H_2O$ or NaHSe (prepared by mixing 8 mg of $NaBH_4$ and 16 mg of Se) in 1 mL of water was added into the above flask slowly and further aged for 2 h. DCM and water was then added into the reaction vessel where nanoparticles were collected from the DCM phase via rotary evaporation and rinsed extensively with methanol. The nanoparticles could be readily dispersed in nonpolar solvents such as DCM, THF, and toluene but not in polar solvents like alcohols and acetone.

EPT-capped nanoparticles were prepared in the same manner except that an equal amount of EPT was used instead of EPA.

Characterizations. TEM images were acquired with a Tecnai G2 instrument operated at 200 kV. SEM and EDS-based elemental mapping analysis was carried out with an Apreo SEM microscope. XRD patterns were collected with a Bruker D8 Advance diffractometer using Cu Kα radiation (λ = 0.15418 nm). XPS measurements were carried out with a Thermo Fisher K-α system. Raman measurements were conducted by using a Horiba Jobin Yvon LabRAM ARAMIS automated scanning confocal Raman microscope under 532 nm excitation. FTIR spectra were collected with a PerkinElmer FTIR spectrometer (Spectrum One), where the samples were prepared by drop-casting the nanoparticle solutions in DCM onto a NaCl disk. UV−vis absorption measurements were carried out with a PerkinElmer Lambda 35 UV−vis spectrometer, and photoluminescence studies were performed with a PTI fluorospectrometer. ^{1}H NMR spectra were acquired with a Bruker Avance III HD 800 MHz spectrometer by using concentrated solutions of the nanoparticles in CD_2Cl_2. XAS measurements were carried out at 10 K at beamline 4−1 of the Stanford Synchrotron Radiation Lightsource

https://doi.org/10.1021/acs.inorgchem.3c03386
Inorg. Chem. 2024, 63, 1046−1053

using an Oxford liquid helium cryostat. The fitting of XAS data was done by using the Real-Space X-ray Absorption Package (RSXAP).

Calculations. Geometric optimization, vibrational frequency, and TD-DFT calculation of alkyne and associated Pt molecules were performed on ORCA 5.0 with the B3LYP functional and def2-TZVP basis set for all elements.[44] For Bader charge analysis and DOS analysis, first-principles computations were performed using Quantum ESPRESSO, an open-source plane-wave code.[45] A unit cell with 4 layers and 64 atoms was used to build a PtS (211) slab supercell, and a unit cell with 4 layers and 56 atoms was used to build a Pt_5Se_4 (006) slab, where periodic image interactions were removed by setting a vacuum of 20 Å. Bottom 2 layers of all models were fixed to simulate the bulk properties. A cutoff of 40 and 240 Ry for kinetics and charge density was chosen with the ultrasoft pseudopotential.[46] The total energy of the Monkhorst−Pack 2 × 3 × 1 K point grid in the supercell was calculated at the convergence level of 1 meV per atom for both PtS and Pt_5Se_4 cases. The smearing parameter was set at 0.01 Ry in the Marzari Vanderbilt smearing for all calculations.[47] For geometric relaxation, the convergence was 10^{-8} Ry of the electronic energy and 10^{-4} au for the total force. The dipole correction was added by applying a finite field to the bare ionic potential for all calculations involving ligand modification.

■ ASSOCIATED CONTENT

Supporting Information

The Supporting Information is available free of charge at https://pubs.acs.org/doi/10.1021/acs.inorgchem.3c03386.

> Additional experimental and computational data; photographs of solutions with nanoparticles; corresponding TEM images and size distributions of nanoparticles; XRD; EDS analysis; additional XPS analysis; computational details of models; DOS and PDOS studies; FTIR and calculated FTIR spectra; ^{1}H NMR, EXAFS fitting details; and simulated EXAFS; additional PL spectra of EPA monomers and Pt−EPA complexes; experimental and theoretical IR spectra of Pt−EPA complexes; synthesis and characterizations of Ru chalcogenide (S, Se) nanoparticles; tables of XPS fittings and XAS fittings (PDF)

■ AUTHOR INFORMATION

Corresponding Author

Shaowei Chen − *Department of Chemistry and Biochemistry, University of California, Santa Cruz, California 95064, United States;* orcid.org/0000-0002-3668-8551; Email: shaowei@ucsc.edu

Authors

Qiming Liu − *Department of Chemistry and Biochemistry, University of California, Santa Cruz, California 95064, United States;* orcid.org/0000-0001-5839-5453

Xingjian Song − *Department of Chemistry and Biochemistry, University of California, Santa Cruz, California 95064, United States*

Davida DuBois − *Department of Chemistry and Biochemistry, University of California, Santa Cruz, California 95064, United States;* orcid.org/0000-0002-2612-3717

Bingzhe Yu − *Department of Chemistry and Biochemistry, University of California, Santa Cruz, California 95064, United States*

Amrinder Bhuller − *Department of Chemistry and Biochemistry, University of California, Santa Cruz, California 95064, United States*

Gabriel Flannery − *Department of Chemistry and Biochemistry, University of California, Santa Cruz, California 95064, United States*

Marcus Hawley − *Department of Chemistry and Biochemistry, University of California, Santa Cruz, California 95064, United States*

Frank Bridges − *Department of Physics, University of California, Santa Cruz, California 95064, United States*

Complete contact information is available at: https://pubs.acs.org/10.1021/acs.inorgchem.3c03386

Author Contributions

[§]Q.L. and X.S. contributed equally to this work. The manuscript was written through contributions of all authors. All authors have given approval to the final version of the manuscript.

Notes

The authors declare no competing financial interest.

■ ACKNOWLEDGMENTS

This work was supported by the National Science Foundation (CHE-1900235 and CHE-2003685). TEM, XPS, and Raman studies were conducted as part of a user project at the National Center for Electron Microscopy and Molecular Foundry, Lawrence Berkeley National Laboratory, which is supported by the Office of Science, Office of Basic Energy Sciences of the U.S. Department of Energy under Contract No. DE-AC02-05CH11231. The authors thank Dr. L. Klivansky at Lawrence Berkeley National Laboratory for the assistance in IR measurements. XAS experiments were performed at the Stanford Synchrotron Radiation Lightsource (SSRL), which is supported by the U.S. Department of Energy, Office of Science, Office of Basic Energy Sciences under Contract No. DE-AC02-76SF00515. Computational work was carried out using the Lux supercomputer at UCSC which is funded by the NSF MRI program (AST-1828315). The authors also thank Mr. J. Barnett for the assistance in sample preparation and data collection in XRD experiments. The XRD Facility was funded by the National Science Foundation (MRI-1126845).

■ REFERENCES

(1) Zhang, Y.; Zhou, Q.; Zhu, J. X.; Yan, Q. Y.; Dou, S. X.; Sun, W. P. Nanostructured Metal Chalcogenides for Energy Storage and Electrocatalysis. *Adv. Funct Mater.* **2017**, *27* (35), 1702317.

(2) Chen, H.; Ran, M. Y.; Wei, W. B.; Wu, X. T.; Lin, H.; Zhu, Q. L. A comprehensive review on metal chalcogenides with three-dimensional frameworks for infrared nonlinear optical applications. *Coord. Chem. Rev.* **2022**, *470*, 214706 DOI: 10.1016/j.ccr.2022.214706.

(3) Chung, I.; Kanatzidis, M. G. Metal Chalcogenides: A Rich Source of Nonlinear Optical Materials. *Chem. Mater.* **2014**, *26* (1), 849−869.

(4) Kershaw, S. V.; Susha, A. S.; Rogach, A. L. Narrow bandgap colloidal metal chalcogenide quantum dots: synthetic methods, heterostructures, assemblies, electronic and infrared optical properties. *Chem. Soc. Rev.* **2013**, *42* (7), 3033−3087.

(5) Zhou, J. D.; Lin, J. H.; Huang, X. W.; Zhou, Y.; Chen, Y.; Xia, J.; Wang, H.; Xie, Y.; Yu, H. M.; Lei, J. C.; Wu, D.; Liu, F. C.; Fu, Q. D.; Zeng, Q. S.; Hsu, C. H.; Yang, C. L.; Lu, L.; Yu, T.; Shen, Z. X.; Lin, H.; Yakobson, B. I.; Liu, Q.; Suenaga, K.; Liu, G. T.; Liu, Z. A library of atomically thin metal chalcogenides. *Nature* **2018**, *556* (7701), 355−359.

(6) Cao, X. Y.; Ding, C. P.; Zhang, C. L.; Gu, W.; Yan, Y. H.; Shi, X. H.; Xian, Y. Z. Transition metal dichalcogenide quantum dots:

synthesis, photoluminescence and biological applications. *J. Mater. Chem. B* **2018**, *6* (48), 8011−8036.
(7) Cordones, A. A.; Scheele, M.; Alivisatos, A. P.; Leone, S. R. Probing the Interaction of Single Nanocrystals with Inorganic Capping Ligands: Time-Resolved Fluorescence from CdSe-CdS Quantum Dots Capped with Chalcogenidometalates. *J. Am. Chem. Soc.* **2012**, *134* (44), 18366−18373.
(8) Giansante, C. Library Design of Ligands at the Surface of Colloidal Nanocrystals. *Acc. Chem. Res.* **2020**, *53* (8), 1458−1467.
(9) Hendricks, M. P.; Campos, M. P.; Cleveland, G. T.; Jen-La Plante, I.; Owen, J. S. A tunable library of substituted thiourea precursors to metal sulfide nanocrystals. *Science* **2015**, *348* (6240), 1226−1230.
(10) Lhuillier, E.; Pedetti, S.; Ithurria, S.; Nadal, B.; Heuclin, H.; Dubertret, B. Two-Dimensional Colloidal Metal Chalcogenides Semiconductors: Synthesis, Spectroscopy, and Applications. *Acc. Chem. Res.* **2015**, *48* (1), 22−30.
(11) Mourdikoudis, S.; Menelaou, M.; Fiuza-Maneiro, N.; Zheng, G. C.; Wei, S. Y.; Perez-Juste, J.; Polavarapu, L.; Sofer, Z. Oleic acid/oleylamine ligand pair: a versatile combination in the synthesis of colloidal nanoparticles. *Nanoscale Horiz.* **2022**, *7* (9), 941−1015, DOI: 10.1039/D2NH00111J.
(12) Bertolotti, F.; Dirin, D. N.; Ibanez, M.; Krumeich, F.; Cervellino, A.; Frison, R.; Voznyy, O.; Sargent, E. H.; Kovalenko, M. V.; Guagliardi, A.; Masciocchi, N. Crystal symmetry breaking and vacancies in colloidal lead chalcogenide quantum dots. *Nat. Mater.* **2016**, *15* (9), 987−994.
(13) González, P. T.; Correa, C. E.; Bonilla, C. A. Aqueous-phase synthesized CdTe quantum dots: an insight into nanoparticle architecture-quantum yield relationship, characterization, and computational study of small clusters. *New J. Chem.* **2022**, *46* (44), 21301−21310.
(14) Kennehan, E. R.; Munson, K. T.; Grieco, C.; Doucette, G. S.; Marshall, A. R.; Beard, M. C.; Asbury, J. B. Influence of Ligand Structure on Excited State Surface Chemistry of Lead Sulfide Quantum Dots. *J. Am. Chem. Soc.* **2021**, *143* (34), 13824−13834.
(15) Yazdani, N.; Volk, S.; Yarema, O.; Yarema, M.; Wood, V. Size, Ligand, and Defect-Dependent Electron-Phonon Coupling in Chalcogenide and Perovskite Nanocrystals and Its Impact on Luminescence Line Widths. *ACS Photonics* **2020**, *7* (5), 1088−1095.
(16) Li, G.; Jin, R. C. Gold Nanocluster-Catalyzed Semihydrogenation: A Unique Activation Pathway for Terminal Alkynes. *J. Am. Chem. Soc.* **2014**, *136* (32), 11347−11354.
(17) Zhang, F. Q.; Fang, J. J.; Huang, L.; Sun, W. M.; Lin, Z.; Shi, Z. Q.; Kang, X. W.; Chen, S. W. Alkyne-Functionalized Ruthenium Nanoparticles: Impact of Metal-Ligand Interfacial Bonding Interactions on the Selective Hydrogenation of Styrene. *ACS Catal.* **2019**, *9* (1), 98−104.
(18) Chen, W.; Zuckerman, N. B.; Kang, X. W.; Ghosh, D.; Konopelski, J. P.; Chen, S. W. Alkyne-Protected Ruthenium Nanoparticles. *J. Phys. Chem. C* **2010**, *114* (42), 18146−18152.
(19) Kang, X. W.; Zuckerman, N. B.; Konopelski, J. P.; Chen, S. W. Alkyne-Stabilized Ruthenium Nanoparticles: Manipulation of Intraparticle Charge Delocalization by Nanoparticle Charge States. *Angew. Chem., Int. Ed.* **2010**, *49* (49), 9496−9499.
(20) Peng, Y.; Liu, Q. M.; Lu, B. Z.; He, T.; Nichols, F.; Hu, X.; Huang, T.; Huang, G.; Guzman, L.; Ping, Y.; Chen, S. W. Organically Capped Iridium Nanoparticles as High-Performance Bifunctional Electrocatalysts for Full Water Splitting in Both Acidic and Alkaline Media: Impacts of Metal-Ligand Interfacial Interactions. *ACS Catal.* **2021**, *11* (3), 1179−1188.
(21) Peng, Y.; Hirata, E. Y.; Pan, W. Z.; Chen, L. M.; Lu, J. E.; Chen, S. W. Intraparticle Charge Delocalization through Conjugated Metal-Ligand Interfacial Bonds: Effects of Metal d Electrons. *Chin. J. Chem. Phys.* **2018**, *31* (4), 433−438.
(22) Purkait, T. K.; Iqbal, M.; Wahl, M. H.; Gottschling, K.; Gonzalez, C. M.; Islam, M. A.; Veinot, J. G. C. Borane-Catalyzed Room-Temperature Hydrosilylation of Alkenes/Alkynes on Silicon Nanocrystal Surfaces. *J. Am. Chem. Soc.* **2014**, *136* (52), 17914−17917.
(23) Kelly, J. A.; Veinot, J. G. C. An Investigation into Near-UV Hydrosilylation of Freestanding Silicon Nanocrystals. *ACS Nano* **2010**, *4* (8), 4645−4656.
(24) Ashby, S. P.; Thomas, J. A.; Garcia-Canadas, J.; Min, G.; Corps, J.; Powell, A. V.; Xu, H. L.; Shen, W.; Chao, Y. M. Bridging silicon nanoparticles and thermoelectrics: phenylacetylene functionalization. *Faraday Discuss.* **2014**, *176*, 349−361.
(25) Peng, Y.; Lu, B. Z.; Wu, F.; Zhang, F. Q.; Lu, J. E.; Kang, X. W.; Ping, Y.; Chen, S. W. Point of Anchor: Impacts on Interfacial Charge Transfer of Metal Oxide Nanoparticles. *J. Am. Chem. Soc.* **2018**, *140* (45), 15290−15299.
(26) Liu, Q. M.; Peng, Y.; Masood, Z.; DuBois, D.; Tressel, J.; Nichols, F.; Ashby, P.; Mercado, R.; Assafa, T.; Pan, D. J.; Kuo, H. L.; Lu, J. Q.; Bridges, F.; Millhauser, G.; Ge, Q. F.; Chen, S. W. Stable Cuprous Hydroxide Nanostructures by Organic Ligand Functionalization. *Adv. Mater.* **2023**, *35* (8), 2208665.
(27) Collins, R.; Kaner, R.; Russo, P.; Wold, A.; Avignant, D. High-Pressure Phase-Transformation of Platinum Sulfide. *Inorg. Chem.* **1979**, *18* (3), 727−729.
(28) Matković, P.; Schubert, K. Kristallstruktur von Pt5Se4. *J. Less-Common Met.* **1977**, *55* (2), 185−190, DOI: 10.1016/0022-5088(77)90191-6.
(29) Yu, B. Z.; Liu, Q. M.; Nichols, F.; Mayford, K.; Pan, D. J.; Kuo, H. L.; Lu, J. Q.; Bridges, F.; Chen, S. W. Platinum-Anchored Iron Oxide Nanostructures for Efficient Hydrogen Evolution Reaction in Acidic Media. *J. Phys. Chem. C* **2023**, *127* (8), 3996−4005.
(30) Andersson, K. J.; Ogasawara, H.; Nordlund, D.; Brown, G. E.; Nilsson, A. Preparation, Structure, and Orientation of Pyrite FeS2{100} Surfaces: Anisotropy, Sulfur Monomers, Dimer Vacancies, and a Possible FeS Surface Phase. *J. Phys. Chem. C* **2014**, *118* (38), 21896−21903.
(31) Lin, S. H.; Liu, Y.; Hu, Z. X.; Lu, W.; Mak, C. H.; Zeng, L. H.; Zhao, J.; Li, Y. Y.; Yan, F.; Tsang, Y. H.; Zhang, X. M.; Lau, S. P. Tunable active edge sites in PtSe2 films towards hydrogen evolution reaction. *Nano Energy* **2017**, *42*, 26−33.
(32) Xue, X. L.; Song, X. M.; Yan, W.; Jiang, M. H.; Li, F. J.; Zhang, X. L.; Tie, Z. X.; Jin, Z. Cooperative Cationic and Anionic Redox Reactions in Ultrathin Polyvalent Metal Selenide Nanoribbons for High-Performance Electrochemical Magnesium-Ion Storage. *ACS Appl. Mater. Interfaces* **2022**, *14* (43), 48734−48742.
(33) Chen, E.; Xu, W.; Chen, J.; Warner, J. H. 2D layered noble metal dichalcogenides (Pt, Pd, Se, S) for electronics and energy applications. *Mater. Today Adv.* **2020**, *7*, 100076.
(34) Liu, Q. M.; Peng, Y.; Li, Q. X.; He, T.; Morris, D.; Nichols, F.; Mercado, R.; Zhang, P.; Chen, S. W. Atomic Dispersion and Surface Enrichment of Palladium in Nitrogen-Doped Porous Carbon Cages Lead to High-Performance Electrocatalytic Reduction of Oxygen. *ACS Appl. Mater. Interfaces* **2020**, *12* (15), 17641−17650.
(35) Kempt, R.; Kuc, A.; Heine, T. Two-Dimensional Noble-Metal Chalcogenides and Phosphochalcogenides. *Angew. Chem., Int. Ed.* **2020**, *59* (24), 9242−9254.
(36) Wang, Y. L.; Li, L. F.; Yao, W.; Song, S. R.; Sun, J. T.; Pan, J. B.; Ren, X.; Li, C.; Okunishi, E.; Wang, Y. Q.; Wang, E. Y.; Shao, Y.; Zhang, Y. Y.; Yang, H. T.; Schwier, E. F.; Iwasawa, H.; Shimada, K.; Taniguchi, M.; Cheng, Z. H.; Zhou, S. Y.; Du, S. X.; Pennycook, S. J.; Pantelides, S. T.; Gao, H. J. Monolayer $PtSe_2$, a New Semiconducting Transition-Metal-Dichalcogenide, Epitaxially Grown by Direct Selenization of Pt. *Nano Lett.* **2015**, *15* (6), 4013−4018.
(37) Back, S.; Gossage, R. A.; Rheinwald, G.; del Rio, I.; Lang, H.; van Koten, G. Titanium alpha-acetylides as building blocks for heterobimetallic transition metal complexes: synthesis and redox behaviour of pi-conjugated organometallic systems. *J. Organomet. Chem.* **1999**, *582* (1), 126−138.
(38) Hu, P. G.; Chen, L. M.; Deming, C. P.; Bonny, L. W.; Lee, H. W.; Chen, S. W. Identification of the formation of metal-vinylidene interfacial bonds of alkyne-capped platinum nanoparticles by isotopic labeling. *Chem. Commun.* **2016**, *52* (78), 11631−11633.

https://doi.org/10.1021/acs.inorgchem.3c03386
Inorg. Chem. 2024, 63, 1046−1053

(39) Kang, X. W.; Zuckerman, N. B.; Konopelski, J. P.; Chen, S. W. Alkyne-Functionalized Ruthenium Nanoparticles: Ruthenium-Vinylidene Bonds at the Metal-Ligand Interface. *J. Am. Chem. Soc.* **2012**, *134* (3), 1412−1415.
(40) Yin, S. Q.; Zhang, W. T.; Tan, C. Y.; Chen, L. J.; Chen, J. W.; Li, G.; Zhang, H. L.; Zhang, Y.; Wang, W. K.; Li, L. Thermal Conductivity of Few-Layer PtS2 and PtSe2 Obtained from Optothermal Raman Spectroscopy. *J. Phys. Chem. C* **2021**, *125* (29), 16129−16135.
(41) Li, Z. C.; Huang, M. R.; Li, J.; Zhu, H. W. Large-Scale, Controllable Synthesis of Ultrathin Platinum Diselenide Ribbons for Efficient Electrocatalytic Hydrogen Evolution. *Adv. Funct. Mater.* **2023**, *33* (28), 2300376.
(42) Creighton, J. A.; Eadon, D. G. Ultraviolet Visible Absorption-Spectra of the Colloidal Metallic Elements. *J. Chem. Soc., Faraday Trans.* **1991**, *87* (24), 3881−3891, DOI: 10.1039/FT9918703881.
(43) Díaz, D.; Castillo-Blum, S. E.; Alvarez-Fregoso, O.; Rodriguez-Gattorno, G.; Santiago-Jacinto, P.; Rendon, L.; Ortiz-Frade, L.; Leon-Paredes, Y. J. Synthesis and characterization of RuS2 nanostructures. *J. Phys. Chem. B* **2005**, *109* (48), 22715−22724.
(44) Neese, F. Software update: The ORCA program system-Version 5.0. *Wiley Interdiscip. Rev.: Comput. Mol. Sci.* **2022**, *12* (5), e1606 DOI: 10.1002/wcms.1606.
(45) Giannozzi, P.; Baroni, S.; Bonini, N.; Calandra, M.; Car, R.; Cavazzoni, C.; Ceresoli, D.; Chiarotti, G. L.; Cococcioni, M.; Dabo, I.; Dal Corso, A.; de Gironcoli, S.; Fabris, S.; Fratesi, G.; Gebauer, R.; Gerstmann, U.; Gougoussis, C.; Kokalj, A.; Lazzeri, M.; Martin-Samos, L.; Marzari, N.; Mauri, F.; Mazzarello, R.; Paolini, S.; Pasquarello, A.; Paulatto, L.; Sbraccia, C.; Scandolo, S.; Sclauzero, G.; Seitsonen, A. P.; Smogunov, A.; Umari, P.; Wentzcovitch, R. M. QUANTUM ESPRESSO: a modular and open-source software project for quantum simulations of materials. *J. Phys.: Condens. Matter* **2009**, *21* (39), 395502.
(46) Garrity, K. F.; Bennett, J. W.; Rabe, K. M.; Vanderbilt, D. Pseudopotentials for high-throughput DFT calculations. *Comput. Mater. Sci.* **2014**, *81*, 446−452.
(47) Marzari, N.; Vanderbilt, D.; De Vita, A.; Payne, M. C. Thermal Contraction and Disordering of the Al(110) Surface. *Phys. Rev. Lett.* **1999**, *82* (16), 3296−3299.

https://doi.org/10.1021/acs.inorgchem.3c03386
Inorg. Chem. 2024, 63, 1046−1053